Green Chemistry

PAPER

View Article Online
View Journal | View Issue

Cite this: *Green Chem.*, 2024, **26**, 8330

Highly efficient production of 2,3-pentanedione from condensation of bio-derived lactic acid over polymorphic ZrO_2†

Neha Dhiman,[a,b] B. Moses Abraham,[c] Deepti Agrawal,[b,d] Sudhakara Reddy Yenumala,[b,e] Jyoti Porwal[d] and Bipul Sarkar *[a,b]

Received 29th April 2024,
Accepted 5th June 2024

DOI: 10.1039/d4gc02097a

rsc.li/greenchem

The demand for fermentation-based chemicals is expected to grow in the coming years because of the increasing emphasis on using bio-based chemicals over petrochemicals. Growing crude oil prices and rising concerns about carbon discharge are the main reasons pushing the shift toward bio-based chemicals. 2,3-Pentanedione is one such high-value fine chemical that is currently produced in smaller quantities through a multi-stage chemical synthesis or extracted from milk waste. Here we report a green route to produce 2,3–pentanedione directly from vapour-phase condensation of crude lactic acid over polymorphic ZrO_2. The catalyst exhibits high selectivity, activity and stability for the direct condensation of raw lactic acid to 2,3-pentanedione and achieved 99.7% LA conversion and 95.5% selectivity at 325 °C.

Introduction

Conversion technologies that produce fuels and chemicals from abundant, renewable biomass and its by-products represent a viable alternative to reducing dependence on fossil fuels.[1–3] Compared to oil, coal, and natural gas, biomass contains low or trace amounts of sulfur or nitrogenous compounds; this makes it a clean and renewable source of carbon.[4] In recent years, the synthesis of chemicals from biomass or bio-derived products has become a hot research topic.[5,6] Apparently, fermentation of agricultural or food waste/substrates is a sustainable alternative for producing specific chemicals and fuel currently made from fossil sources.[7,8] The fermentation technology uses carbonaceous waste and sugar as sources of nutrients and energy; the microbes then produce diverse products, including low-carbon fuels and high-value chemicals for everyday applications. Lactic acid is one such end product of the fermentation of sugar cane bagasse (SCB) using the thermophilic *Bacillus coagulans* NCIM 5648.[9] This fermented end product can be converted into fine chemicals over a suitable heterogeneous catalyst. Our previous study demonstrated that this biologically derived lactic acid could be converted into acrylic acid, an environmentally friendly and sustainable process to produce industrially relevant acrylic acid in high yield.[7] Overall, bio-derived lactic acid (LA) is particularly appealing due to its simple synthesis *via* biomass fermentation, as well as the expected increased availability and lower cost.[10,11] Several studies have been conducted to convert LA to chemicals such as acrylic acid, pyruvic acid,[12,13] propionic acid,[14] acetaldehyde, poly(lactic acid), and 2,3-pentanedione.[15] However, the raw lactic acid must be further purified to technical or analytical grade before being used in this described process. This is a crucial issue for its commercial application as it increases the operating costs of the intended process. Therefore, efforts must be made to develop a simple catalytic process to process crude lactic acid directly from fermentation or chemical production units.

Lactic acid can undergo multiple reactions to produce potentially valuable compounds as it contains both hydroxyl and carboxylate functional groups. Fig. 1 illustrates different conversion pathways of LA. Among these, the specialty chemical 2,3-pentanedione is generally used as an artificial flavouring in the food industry.[16] It is also used as a solvent in paints, inks, and varnishes, and as a feedstock for synthesising duroquinone, bisphenols, and pyrazines.[17,18] Therefore there is a profitable opportunity if it can be produced sustainably. Commercially, 2,3-pentanedione is manufactured *via* the oxidation of methyl propyl ketone with hydroxylamine hydrochloride over $NaNO_2$ and HCl as the catalyst.[19] Hydroxyacetone (acetol) condensation with hexanal, accelerated by acid, can

[a]*Catalytic De-Polymerization Area, Upstream & Wax Rheology Division, CSIR- Indian Institute of Petroleum, Haridwar Road, Dehradun-248005, India. E-mail: bsarkar@iip.res.in*
[b]*Academy of Scientific and Innovative Research (AcSIR), CSIR-HRDC Campus, Joggers Road, Kamla Nehru Nagar, Ghaziabad-201 002, India.*
[c]*Department of Chemical Engineering, Indian Institute of Technology Kanpur, Kanpur, 208016, India*
[d]*Biochemistry and Biotechnology Area, Material Resource Efficiency Division, CSIR-Indian Institute of Petroleum, Dehradun 248005, India*
[e]*Biofuels Esterification Area, Bio Fuels Division, CSIR-Indian Institute of Petroleum, Dehradun 248005, India*
† Electronic supplementary information (ESI) available. See DOI: https://doi.org/10.1039/d4gc02097a

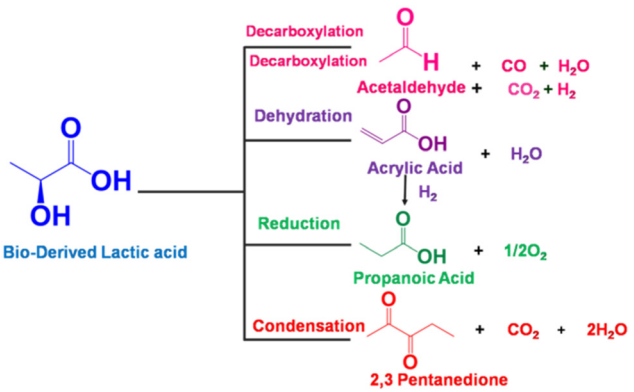

Fig. 1 Primary conversion pathway of lactic acid.

also yield 2,3-pentanedione. 2,3-Pentanedione *via* catalytic vapour-phase condensation of LA is concentrated chiefly on carbon/silicon supported by alkali–metal nitrates or phosphates as catalysts.[15,20,21] Among them, a few catalysts produce 2,3-pentanedione as a side product and proceed to acetaldehyde and acrylic acid through the decarbonylation and hydration of LA, respectively. Therefore, the relationship between the acid–base properties and catalytic activity must be fully understood to increase the reactivity, 2,3-pentanedione selectivity, and area-specific catalytic rate. According to Huang *et al.*, two crucial steps involve intermediate dehydration and decarboxylation in the hypothesised reaction pathway for LA to 2,3-pentanedione.[22] Decarboxylation needs mild basic sites, whereas dehydration needs weak to medium acidic sites. Therefore, the catalytic condensation of LA must require both acidic and basic sites available on the catalyst's surface.[15] Accordingly, this work uses carbon pillared zirconia polymorph as a catalyst for the vapour phase condensation of crude lactic acid. It is well documented that both acidic and basic sites are found on porous carbons.[23] We implemented a different approach for synthesising carbon pillared zirconium oxide. Here, the catalytic account of structural carbon remarkably adjusts the acid–base properties of the catalyst to achieve a staggering 95.3% yield of 2,3-pentanedione.

Experimental

Feedstock

Lactic acid (L-isomer) was produced using a homo-fermentative and thermophilic *Bacillus coagulans* NCIM 5648, purchased from the National Collection of Industrial Microorganisms (NCIM), India. The enzymatic saccharification of alkali-pretreated SCB was performed with Cellic CTec2 using an optimised strategy.[24] Later, sugar-rich enzymatic hydrolysate (≥165 g L^{-1} glucose and xylose) was valorised to L(+)lactic acid using *B. coagulans* NCIM 5648 under pH-controlled conditions, as described earlier.[9] The fermentation was terminated when the broth's glucose was completely exhausted.

The cell-free, lactic acid-rich broth was obtained by centrifugation at 7500 rpm for 10 min at 4 °C. This lactic acid obtained from SCB was the starting material for vapour-phase condensation toward 2,3-pentanedione. The broth was appropriately diluted to conduct the condensation experiments.

Materials

An aqueous solution of ~20% crude lactic acid (as stated above) was utilised in all experiments. Zirconium oxychloride octahydrate ($ZrOCl_2{\cdot}8H_2O$), D-glucose ($C_6H_{12}O_6$), and orthophosphoric acid (H_3PO_4, 88%) were purchased from SRL Chemical, TCI Chemical, and Loba Chemical CO, respectively. High-purity 2,3-pentanedione, propanoic acid, and acetic acid were used as calibration standards. Double-distilled water was prepared in a Borosil® unit in the laboratory.

Catalyst preparation

Zirconium oxide was prepared using a hydrothermal method. Prior to the synthesis, 12.9 g of dextrose was dissolved in 30 ml of distilled water and stirred. Zirconium oxychloride ($ZrOCl_2{\cdot}8H_2O$) (4.64 g) was dissolved in 16 ml of water and stirred for a homogeneous solution. Both the solutions were mixed and stirred overnight at room temperature. Then, the homogeneous solution was placed in a stainless-steel autoclave with a Teflon liner and maintained at 180 °C for 24 h. The resultant solid was filtered, washed with cold water and ethanol several times, and dried at 90 °C. The resulting powder was calcined at 500 °C for 6 h at a heating rate of 5 °C min^{-1} in static air.

Catalyst evaluation

A fixed bed quartz tube reactor with an 8 mm inner diameter operated at atmospheric pressure was used for the vapour-phase condensation of bio-derived lactic acid. SiC_2 was used to make the catalyst bed, and the palletised catalyst (1 g, 30–40 meshes) was placed at the centre of the reactor. The catalyst was pre-heated for 1.5 h in the presence of nitrogen gas (flow rate 20 ml min^{-1}) at 250–375 °C. The feed, *i.e.*, crude lactic acid (~40 wt% solutions) from the fermentation broth, was pumped into the reactor (LHSV = 1–5 h^{-1}). The 250–375 °C range was used to test the catalysts under an N_2 flow of 20 ml min^{-1}. The reaction product was analysed using high-performance liquid chromatography (HPLC) with an Amine-X-HPX-87H column. The conversion of lactic acid and the yield or selectivity towards 2,3-pentanedione were calculated using the following equations:

$$\text{Conversion}_{LA}\,(\%) = \frac{Q_{LA,in} - Q_{LA,out}}{Q_{LA,in}} \times 100\,(\%)$$

$$\text{Selectivity}_{(PD)}(\%) = \frac{Q_{(PD,out)}}{Q_{LA,in} - Q_{LA,out}} \times 100\,(\%)$$

$$(\%)Y_{PD} = \frac{Q_{PD,out}}{Q_{LA,in}} \times 100\,(\%)$$

where Q is the moles of the reactant or product, and LA and PD represent lactic acid and 2,3-pentanedione, respectively.

Furthermore, we confirm that all activities and selectivities are carbon-based and have a mass balance of 93 ± 3%.

Catalyst characterisation

Powder X-ray diffraction (XRD) was performed on a Rigaku Geiger-Flex advanced X-ray diffractometer equipped with a Cu Kα radiation (λ = 0.15418) source at 40 kV and 40 mA. The diffraction pattern was recorded over 2θ angles from the 5–80° region with a 0.04 step size (step time = 4). Scanning electron microscopy (SEM) images were recorded on an FEI Quanta 200F scanning electron microscope, with a tungsten filament doped with lanthanum hexaboride (LaB_6) as an X-ray source equipped with an explosive trace detector (ETD) in high vacuum mode. Before analysis, a small amount of powdered sample was spread on one side of a conductive double-sided carbon tape; then, a gold coating was applied on the sample to shield the charging effect. A transmission electron microscope (TEM) image was taken on a JEOL JEM 2100 microscope, and a catalyst sample was prepared by increasing the ethanol-dispersed sample on a lacey carbon-coated Cu grid. The BET equation was used to measure the specific surface area at −180 °C using Belsorp equipment (BEL Japan, Inc.). Prior to the measurements, the samples were degassed under vacuum (1×10^{-5} Torr) for 2 h at 200 °C. The BET surface areas were determined from the adsorption data in the relative pressure (P/P_0) range from 0.06 to 0.2. The pore size distributions (PSDs) were calculated from the nitrogen adsorption branch using the Barrett–Joyner–Halenda (BJH) method, and the maximum PSD was considered the average pore size. The pore volume was considered as the volume of liquid nitrogen adsorbed at P/P_0 = *ca.* 1.

The catalyst surface composition was examined by X-Ray Photoelectron Spectroscopy (XPS) using a Thermo Scientific K-Alpha X-ray photoelectron spectrometer. The base pressure in the measurement chamber was maintained at about 7×10^{-10} mbar. The measurements were carried out in fixed transmission mode with a pass energy of 200 eV, resulting in an overall energy resolution of 0.25 eV. A flood gun was applied to compensate for the charging effects. The binding energy scales were re-calibrated based on the sp^2 hybridised C 1s line from graphitic carbon at 284.5 eV. Thermogravimetric analysis (TGA) experiments were carried out on a thermal analyser TA-SDT Q-600. The FT-IR spectrum was obtained on a Bruker IFS25 spectrometer. Before analysis, the samples were ground with potassium bromide and pellets were made using a hydraulic press. Thermal conductivity detectors (TCDs) were used to record the results of NH_3 and CO_2 temperature-programmed desorption (NH_3-TPD) studies on Micromeritics Auto Chem II 2920 apparatus. The amount of NH_3 consumed during the measurement was estimated based on the analysis with a thermal conductivity detector. The gas flow rate was 15 mL min^{-1}. The weight of the sample was 25 mg, and the heating rate of TPD was 10 °C min^{-1}. A Horiba Jobin Yvon HR 800UV apparatus was used to conduct Raman studies using a laser with a wavelength of 632.8 nm (λL).

Kinetic study

The condensation of lactic acid was carried out at 300–350 °C under air pressure for the kinetics study. The rate of reaction and other kinetic parameters were computed at an LA conversion of ≤10% LA. The kinetic behaviour of the ZrO_2 catalyst was demonstrated as a function of lactic acid partial pressure and temperature. The expression is as follows:

$$\text{Rate of lactic acid consumption} = \frac{\text{conv. of LA} \times \text{flow rate of LA}}{\text{weight of catalyst}}$$

Experiments were conducted at various initial reactant concentrations, and the initial rates were estimated by differentiating the data. All calculations were performed in the kinetic regime, assuming no or negligible effect of temperature at 10% LA conversion. After one hour, the sample was taken to guarantee the catalyst's steady state and stable performance.

Computational details

The Vienna *Ab initio* Simulation Package[25] was employed to perform density functional theory (DFT) calculations in conjunction with the GGA (generalised gradient approximation) based exchange–correlation functional proposed by Perdew, Burke, and Emzerhof (PBE).[26] The projector-augmented wave approach was used to account for the effect of the core electrons.[27] The plane wave basis set was utilised to compute the valence electron density, where the kinetic energy cut-off was set to 480 eV. The structural relaxation of the ZrO_2 nanocluster was performed at the Γ-point, allowing all the atoms to relax freely until the self-consistency of the electron density and ionic forces was less than 10^{-5} eV and 0.01 eV $Å^{-1}$, respectively. To generate chemically stoichiometric $Zr_{16}O_{32}$ nanoparticles, the relaxed tetragonal ZrO_2 structure was cleaved along the oxygen terminated (101) surface. A vacuum width of 15 Å was used in the out-of-plane Z-direction to separate from their period images. The DFT-D3 method[28] that describes the van der Waals was incorporated to account for the weak intermolecular interactions. The nudged elastic band (NEB) approach represents the reaction coordinate. The PBE+U approach was employed to partially correct the self-interaction error of the GGA functional with an onsite Coulomb correction of 4 eV for the Zr(4d) states. The binding energy of lactic acid (LA) over the ZrO_2 nanocluster was computed using the following equation:

$$\Delta E = E_{ZrO_2/LA} - E_{ZrO_2} - E_{LA}$$

where $E_{ZrO_2/LA}$, E_{ZrO_2}, and E_{LA} are the total energies of the ZrO_2 nanocluster with and without lactic acid and with the isolated LA molecule, respectively.

Results

The powder X-ray diffraction pattern of ZrO_2 is shown in Fig. 2. The peaks observed at 2θ = 24.7, 28.2, 31.5, 35.1, 40.9, 45.2,

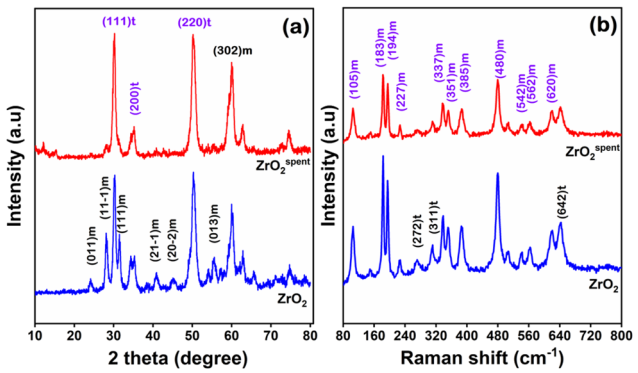

Fig. 2 (a) X-ray diffraction patterns of ZrO_2 and (b) Raman spectra of ZrO_2.

55.4, and 60.1 were assigned to the (011), (11−1), (111), (21−1), (20−2), (013), and (302) reflection planes, respectively, of the monoclinic phase of zirconium oxide.[29] This agrees with the (00-037-1484) standard card from the JCPDS. Meanwhile, the peaks at 2θ of 30.2, 35.3, and 50.3 corresponding to the planes (111), (200) and (220) belong to the tetragonal phase of ZrO_2 (JCPDS no. 00-017-09273). The spent catalyst shows a nominal loss of crystallinity, referring to the disappearance of a few peaks between 40 and 48°. This suggests that the catalyst is stable and has exceptional water tolerance properties. Furthermore, the crystallite size was measured using the Scherrer equation, and the crystallite size of ZrO_2 was found to be 4.5 nm.[30] For the spent catalyst, it was 5 nm, implying no major change in shape and size during the reaction.

To further substantiate the presence of polymorphic phases in ZrO_2, the Raman spectroscopy was recorded and is shown in Fig. 2b. The characteristic peaks at 105, 183, 194, 227, 272, 337, 351, 385, 480, 542, 562, and 620 cm^{-1} are ascribed to the monoclinic phase of ZrO_2.[29,31] Meanwhile, the vibration nodes at 272, 311 and 642 cm^{-1} belong to the tetragonal phase.[31] The XRD and Raman spectroscopy confirm the presence of polymorphism (m-ZrO_2 and t-ZrO_2) phases during hydrothermal synthesis. The Raman spectra of the spent catalyst also confirm no significant changes in its crystal structure, inferring superior water tolerance of the working catalyst. N_2 sorption conforms to type IV isotherms according to the IUPAC classification, suggesting that crystallite stacking leads to the formation of hierarchical pores. The BET surface area and pore volume of the fresh catalyst (Table 1) are 26.34 m^2 g^{-1} and 0.01, respectively. However, the average pore size increased in the case of the spent catalyst, suggesting an enlargement of the pore structure due to the insertion of water/steam during the reaction. This swelling led to the formation of mesopores, as shown in Table 1, but with a loss of surface area. Furthermore, the spent catalyst was reactivated under 5% O_2 balanced N_2 and it was found that the BET surface area increased to 24.8 m^2 g^{-1}. This suggests that the BET surface area does not change significantly in the reactivated catalyst, but pore swelling persists.

Fig. 3 shows the HRTEM images of the ZrO_2 catalysts, which indicate a homogeneous size distribution of ZrO_2 with an average particle size of about 11 nm (Fig. S1†). According to Fig. 3c and f of pure ZrO_2, the lattice fringes have a *d*-spacing value of 2.2 and 3.6 Å, which corresponds to the (21−1) and (011) crystal planes of the monoclinic phase. The crystal plane (111) of the tetragonal phase is represented by the lattice fringes with a *d*-spacing value of 2.5 Å. For ZrO_2, the monoclinic and tetragonal phases are represented by the (200) planes, which correspond to the *d* spacing value at 2.5 Å The SAED images (Fig. 3g–f) also support the observation made in the lattice fringes and the corresponding crystal planes. The SEM image (Fig. S2†) shows a highly agglomerated clumpy coral-like shape. Fig. 4a shows the XPS spectra of Zr 3d, which show two peaks at 181.6 and 184.2 eV that can be assigned to Zr $3d_{5/2}$ and $3d_{3/2}$, respectively.[32,33] This indicates the presence of Zr^{4+}; however, the shift in the binding energy (BE) to lower energies corresponds to the presence of coordinatively unsaturated Zr-species (Zr_{cus}^{x+}). A similar phenomenon was observed by Agrawal *et al.*,[34] and these Zr_{cus} are said to show incredible activity. It was also found that the spin–orbit component was Δ_{oxide} = 2.3 eV, which is 0.1 eV lower than the NIST standard.[35]

Table 1 Acid–base sites calculated based on NH_3/CO_2-TPD and Py-IR of the ZrO_2 catalyst

Catalyst	S_{BET} (m^2 g^{-1})	Pore size (Å)	Pore vol. (cm^3 g^{-1})	Acid strength[a] (mmol g_{cat}^{-1})	(*B*/*L*)[b] ration	Basis strength[c] (mmol g_{cat}^{-1})
ZrO_2^{comm}	22.7	12.1	0.008	0.013	1.00	0.039
ZrO_2	26.3	68.1	0.010	0.024	0.36	0.064
ZrO_2^{spent}	7.7	236.9	0.006	0.019	1.52	0.044
$ZrO_2^{acti.}$	24.8	209.2	0.008	0.020	—	—

[a] Calculated from NH_3-TPD. [b] *B*/*L* ratio was calculated from Py-FTIR data. [c] Calculated from CO_2-TPD. ZrO_2^{acti}-activated spent ZrO_2 with 5%O_2 balance N_2.

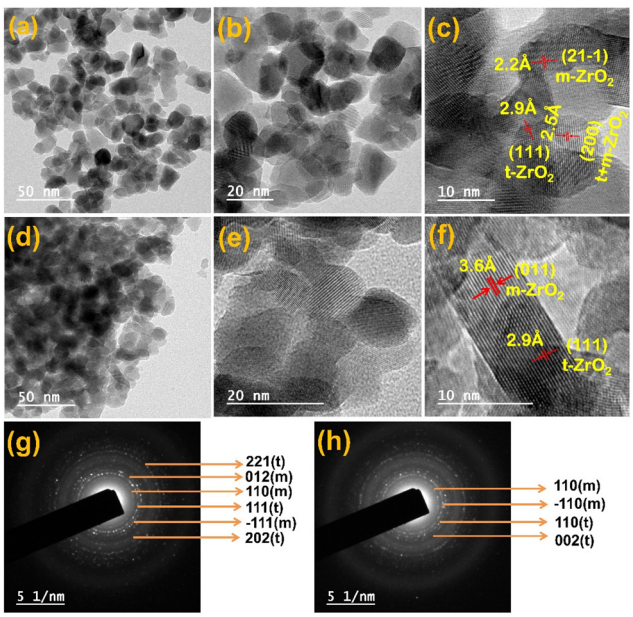

Fig. 3 HR-TEM images (a) fresh and (d–f) spent pure zirconium oxide (ZrO_2); catalysts. The SAED images of (g–h) of fresh and spent ZrO_2.

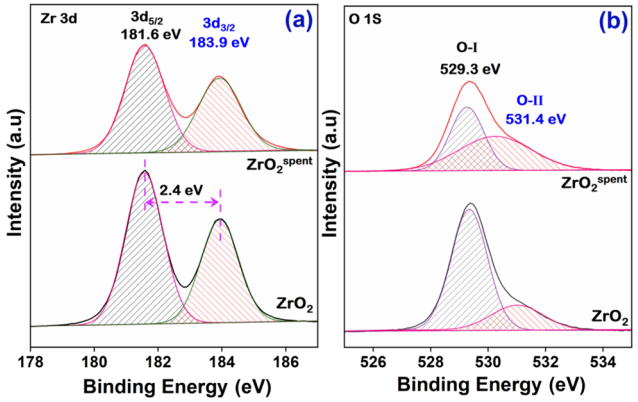

Fig. 4 XPS spectra (a) Zr 3d and (b) O 1s of the ZrO_2 catalyst.

This refers to the small change in the chemical state of prepared ZrO_2 due to the insertion of C and making it coordinatively unsaturated. The XPS spectra of O 1s were deconvoluted into two peaks, as shown in Fig. 4b. The peak at the lower binding energy of 529.3 eV is attributed to the lattice oxygen (O-I), whereas the higher binding energy at 531.4 eV is ascribed to the oxygen (O-II) associated with the lower coordination number/coordinatively unsaturated ions (M_{cus}^{x+}).[32,36] This type of surface now promotes the diffusion of oxygen through atomic assembly since the interstices are the right size for oxygen migration, indicating better oxygen mobility for coke resistance. This leads to lower binding energy values than the monoclinic and tetragonal structures of ZrO_2.[36]

Surface acidity and pyridine-IR

Since decarboxylation and dehydration require weak to moderate acidic and basic sites, acid–base properties in the alignment of catalytic activity must be fully understood to increase reactivity. The surface acidity and basicity of ZrO_2 were characterised using pyridine-adsorbed FTIR, NH_3-TPD and CO_2-TPD, as depicted in Fig. 5 & S3.† The broad and asymmetric features of the NH_3-TPD profiles (Fig. 5a) reveal weak, medium and strong acid sites at <200 °C, >200–400 °C, and >400 °C, respectively.[37,38] The peak at T_{max}-341 °C corresponds to the adsorption of NH_3 on the Zr_{cus} cations associated with the moderately strong acid site. With the catalyst spent, the concentration of the acid sites decreased somewhat, possibly due to the neutralisation of the acid sites by water during the reaction. In connection with the time-on-steam (TOS), it can be said that the acidity rejuvenates with regeneration, and the product distribution remains almost the same up to 20 h. In addition, the calculated acid site strengths are listed in Table 1. For CO_2-TPD in Fig. 5b, the coordinatively unsaturated oxygen-associated Zr_{cus} acts as base sites, whose basicity is also related to the coordination.[39] The profiles were divided into three sections according to the desorption temperature. The formation of bicarbonate is accompanied by the desorption peak at ~200 °C, which is attributed to the weak base site, whereas the moderated sites appear at 200–400 °C. This is attributed to CO_2 adsorption at the moderately strong base site (Zr_{cus}^{x+}–O^{2-} pair), and the strong sites appear >400 °C for the weak coordination O^{2-}, concomitant with the formation of non- or polydentate carbonate. In addition, NH_3-TPD and CO_2-TPD of commercial ZrO_2 have small amounts of Lewis acid–base sites compared to the polymorphic ZrO_2.

This result suggests that more (Zr_{cus}^{x+}–O^{2-} pair) lower-coordination O^{2-} ions are exposed on the ZrO_2 surface. In addition, ZrO_2 adsorbs comparable amounts of CO_2 and NH_3, suggesting the presence of both acidic and basic sites.[40] Among them, the medium-strength Lewis acid–base sites with lower coordination may be exposed, which is the key to this exceptional selectivity/yield.

The pyridine adsorbed on the coordinatively unsaturated Zr^{4+} cations was analysed by FT-IR, and the spectra are shown in Fig. 6a. The py-IR bands at 1604, 1580, 1490, and 1449 cm^{-1} are responsible for the Lewis acid sites (LAS), whereas the band at 1580 cm^{-1} is attributed to the pyridine adsorbed on the hydrogen of the hydroxyl group. The 1630 and 1547 cm^{-1} peaks are typical of Brønsted acid sites (BAS) formed by reacting pyridinium ions with proton sites. The band at 1492 cm^{-1} correlates to both the Lewis and Brønsted acid sites. The *B*/*L* ratio (Table 1) suggests that ZrO_2's surface has a more significant concentration of Lewis acid sites than Brønsted sites, which agrees with the study done by Goyal *et al.*[29] The FTIR spectra

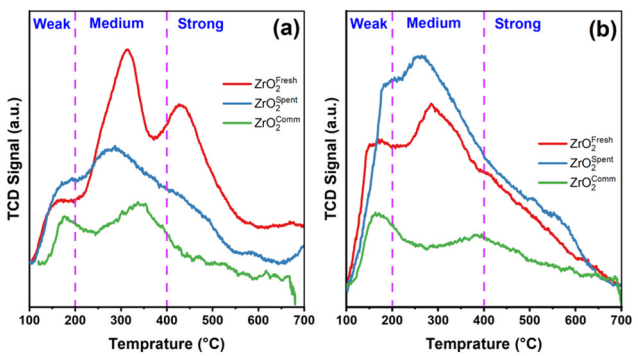

Fig. 5 NH_3-TPD profiles (a) and CO_2-TPD profiles (b) of different ZrO_2 catalysts.

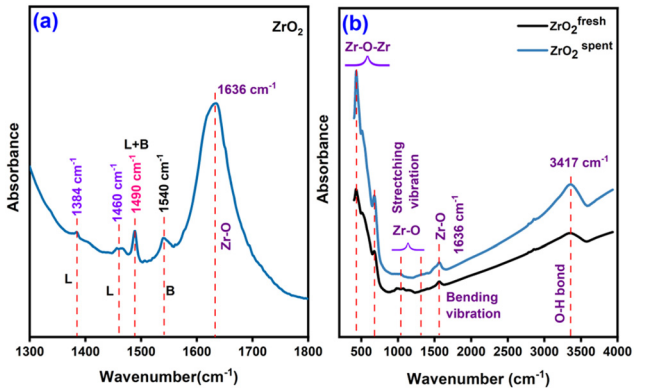

Fig. 6 (a) Pyridine adsorbed FTIR spectra and (b) FTIR graph of ZrO_2.

(Fig. 6b) show a dominant absorption band between 500 and 800 cm^{-1}, which is attributed to the deformation of the Zr–O–Zr bond. Meanwhile, the peak centred around 1040 and 1304 cm^{-1} corresponds to the stretching vibration of Zr–O.[41] The IR bands at 1590 and 1650 cm^{-1} represent the bending vibrations of chemisorbed water molecules along with the O–H stretching at 3445 cm^{-1}, as reported by Prakashbabu *et al.*[42]

Catalytic activity

We first selected raw lactic acid directly from the fermentation broth for the envisioned selective condensation of LA to 2,3-pentanedione. The choice of LA was guided by the possible use of raw lactic acid broth for technological interventions and feasibility. It is not wrong to say that the majority/all of the work done previously has taken lactic acid as a model substrate. Yet, the purification process of crude lactic acid is very laborious on both a small and a large scale.[43] In addition, a large amount of LA from fermentation broth is available in the market at low prices, which can potentially be used as a valuable raw material.[43] Such a sequence would directly lead to the valorisation of crude LA by converting it directly into value-added products using sustainable production processes.

According to the literature, framework zeolites such as MFI and FAU have been investigated (entries 1 and 2).[44,45] However, to boost their basicity, we added a catalytic amount (2 wt%) of Li and Na to the ZSM-5 and Y-zeolite, respectively. The results for Li-ZSM-5 and Na-Y showed 2,3-pentanedione as the major product but with poor 2,3-pentanedione selectivity (entries 1 and 2). In addition, we tried a reaction with acidic MoP and MoS_2 catalysts, but the selectivity of 2,3-pentanedione was very low, and so were the yields (entries 3 and 4). The commercially available ZrO_2 (Sigma Aldrich, entry 5) exhibited a much higher yield of 2,3-pentanedione, among others, although the as-prepared polymorphic ZrO_2 significantly increased the conversion and the selectivity of 2,3-pentanedione compared to the commercial ZrO_2. This could be because the polymorphic ZrO_2 had a slightly higher surface area and porosity (Table 1). Simultaneously, the average particle size of the commercial ZrO_2 was ~100 nm, while the polymorphic ZrO_2 had an average particle size of ~11 nm. Furthermore, the NH_3-TPD and CO_2-TPD data (Fig. 5) show that there were more medium-strength Lewis acid–base sites on the polymorphic ZrO_2 compared to the commercial ZrO_2, which increased the adsorption strength of the lactic acid. A similar observation was also made by Ding *et al.* for the vapor-phase ketonisation of propionic acid over polymorphic ZrO_2.[46] These differences in particle size and acid–base properties affected the adsorption configuration and strength of the lactic acid when compared to the commercial ZrO_2. The higher surface concentration of active sites due to the small particle size and adsorption strength of polymorphic ZrO_2 contributes to the higher condensation rate in the steady state. To further emphasise the behaviour of the different phases of ZrO_2 toward LA condensation, we performed reactions with pure tetragonal and monoclinic ZrO_2. LA condensation at 325 °C over the m-ZrO_2 catalyst shows a LA conversion of 91.5% with 70.5% 2,3-pentanedione selectivity. In the case of the t-ZrO_2 catalyst, it only shows a 2,3-pentanedione selectivity of 44.6%. From the data, it is observable that the phase composition influences the selectivity of 2,3-pentanedione, and the monoclinic phase is more 2,3-pentanedione-oriented than the tetragonal one. It should be noted that the polymorphic ZrO_2 (mostly in the monoclinic phase) causes additional lattice disorder and oxygen vacancies, and with increased acid and basic strength,[47,48] exhibits higher 2,3-pentanedione selectivity. Therefore, it can be stated that both phase compositions, in which the monoclinic phase dominates, were required to achieve maximum condensation of lactic acid to 2,3-pentanedione. Notably, the LA conversion reaches ~99.7%, which is 79.4% over the value for commercial ZrO_2, with a 2,3-pentanedione selectivity of 95.3% at 325 °C. Zhang *et al.* recently observed a 2,3-pentanedione selectivity of 62.1%, at a high reaction temperature of 340 °C, where LA conversion was also low, reaching only 58.8%.[49] The product mixture was analysed by NMR and GC-MS (Fig. S4–S6†) for the identification of 2,3-pentanedione.

Dehydration and decarboxylation are two critical phases for the condensation of LA to 2,3-pentanedione (see Fig. 1, later confirmed by DFT calculation).[22,50] The former reaction requires acid catalysis while the latter requires base catalysis. It is evident from the data in Table 2 that both basic and

Table 2 Comparison studies and product distribution from bio-derived lactic acid over a different synthesised catalyst

		Product selectivity (%)				Yield (%)	TOF[a] (h^{-1})
Catalysts	LA conv. (%)	2,3- Pentanedione	AC	PA	Other		
2Li-ZSM-5	96.1	33.8	12.9	50.2	3.0	33.5	—
Na-Y	63.1	49.9	30.1	17.9	2.0	32.2	—
MoS_2	72.5	63.1	19.6	13.1	4.0	46.5	7.7
MoP	60.1	45.5	16.6	18.9	18.9	28.6	5.8
ZrO_2 ^{comm}	79.4	66.1	7.3	22.1	4.5	52.4	5.6
ZrO_2	99.7	95.5	1.1	2.1	1.1	95.3	6.4
t-ZrO_2	82.5	44.6	10.4	32.3	12.7	36.7	5.9
m-ZrO_2	91.5	70.5	4.2	18.8	14.8	64.2	6.1
2%S-ZrO_2	99.8	68.8	10.8	14.2	6.0	69.7	—

Conditions –feed – ~40 wt% LA solutions, atmospheric pressure, temp. –325 °C. [a] TOF = turnover frequency for lactic acid was calculated at 10–20% lactic acid conversion.

acidic metal moieties were necessary for the reaction. The fact that ZrO_2 is a good catalyst for the condensation of LA to 2,3-pentanedione suggests the presence of suitable acidic and basic sites on its surface. The presence of carbon in ZrO_2 provided better activity than the earlier catalysts. Additionally, GC analysis of tail gas was conducted, and the outcomes are displayed in Fig. S7.† It is striking that CO and H_2 were rarely detected, while CO_2 was detected in significant amounts in the gaseous product. This proves that the condensation of LA is prominent over the carbon–ZrO_2 catalyst over the decarboxylation. Furthermore, it is also worth noting that 2,3-pentanedione is proposed to form by a second-order condensation, while acrylic acid is proposed to result from the elimination of water *via* a cyclic lactic acid–phosphate transition state.[51] Therefore, the involvement of alkali metal and phosphates will start producing acrylic acid (shown as other products) and propanoic acid (PA), which is shown in Table 2. When ZrO_2 was modified with S, the degree of dehydration followed by reduction increased, and a steady increase in PA was observed. Earlier literature findings have suggested that BAS and LAS coexisting could effectively boost the condensation reaction.[52,53] Furthermore, the *B*/*L* ratio indicates that polymorphic ZrO_2 has more LAS, which increases the condensation rate and second reduction process in comparison with the commercial ZrO_2 (Table 2). When the acidity and basicity of the catalyst are considered together to correlate with the catalyst performance, it is shown that higher concentrations of medium acidic and basic sites of the polymorphic ZrO_2 are more selective for condensation than for dehydration or reduction.[52]

Effect of process parameters

Our prior study identified ZrO_2, prepared using dextrose as a template, as an excellent catalyst for condensation of bio-derived lactic acid, which exhibited high 2,3-pentanedione selectivity (95.5 mol%) and yield (95.3 mol%) at 325 °C. Fig. 7a shows the conversion of LA as a function of the reaction temperature. The LA conversion (~99.8%) remained almost constant over the studied temperature (250–375 °C). At the same time, the formation rate (Fig. 7a) showed a slow but steady increase but decreased after 325 °C. The trend indicated that side reactions dominated at higher reaction temperatures (Fig. 7a). In contrast, the selectivity of PA, AC, acrylic acid (represented as other products), and acetaldehyde significantly increased (Fig. 7a), specifically after 325 °C. However, the presence of acrylic acid in small amounts suggests decarbonylation over acidic ZrO_2 sites. Furthermore, the selectivity for 2,3-pentanedione was almost independent (~92–95%) up to 325 °C, but decreased afterwards.

The formation rate of 2,3-pentanedione and the LA consumption (Fig. 8) were dependent on the residence time (relative to LHSV) and increased rapidly. For example, the LA conversion and the rate of 2,3-pentanedione production at 4.0 h^{-1} were 99.9% and 9.52 mmol h^{-1} g^{-1}, respectively, while at 5 h^{-1} they were 99.7% and 9.20 mmol h^{-1} g^{-1}, respectively. The rate of by-product formation increased somewhat with increasing residence time, suggesting that a longer contact time favours the side reactions, which is in strong agreement with previous studies.[54] Furthermore, Table S1† shows some of the previously reported catalysts used for the selective production of 2,3-pentanedione. Expensive alkali metals (Cs) and alkaline earth metals (Ba) are mainly used for LA condensation to 2,3-PDO.[49,55] Moreover, the yield is also between 54 and 65%. As a reference, the polymorphic ZrO_2 used in this study shows high selectivity, activity and stability in the direct condensation of LA to 2,3-pentanedione, achieving 99.7% LA conversion and 95.5% selectivity at 325 °C. Furthermore, in all reported studies, it was found that pure lactic acid was used, and this study was conducted using raw lactic acid from fermentation broth.

Kinetic study

Reaction order in bio-derived lactic acid (LA). The ZrO_2 catalyst has been the subject of thorough kinetic experiments at low LA and low partial pressure (from 0.06 to 0.11 atm). Adsorption, surface, and desorption steps were considered in estimating the reaction rate (R) for each elementary reaction (RDS). As shown in Fig. 9, the reaction order in lactic acid at different temperatures is estimated as the slope of $\ln[p(C_3H_6O_3)]$ *vs.* $\ln[R(C_3H_6O_3)]$. It was found that the formation of 2,3-pentane-

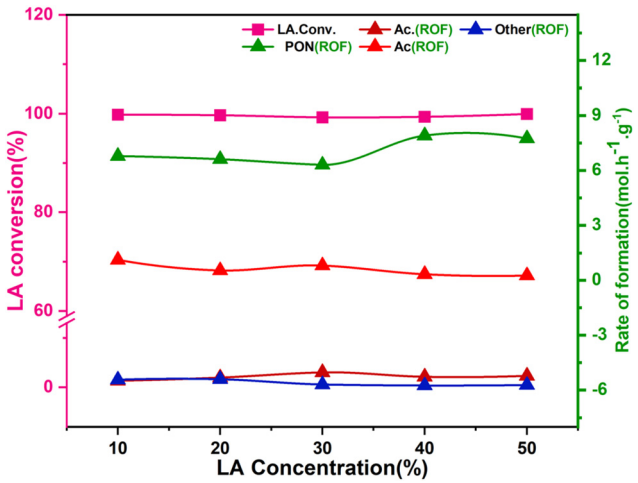

Fig. 7 Effect of (a) temperature and (b) effect of LHSV on the rate of product formation and conversion.

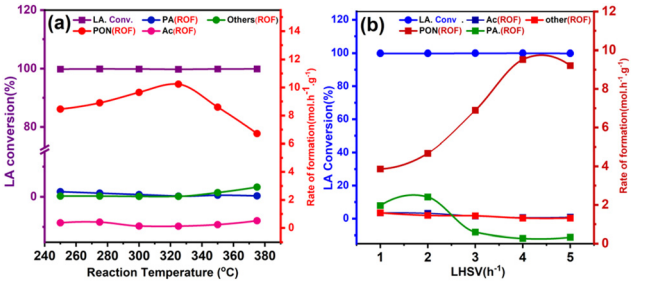

Fig. 8 Effect of lactic acid concentration on the rate of product formation and conversion.

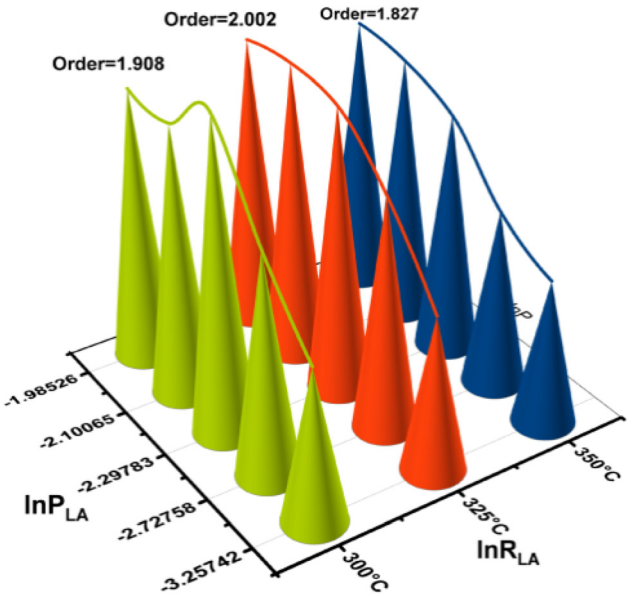

Fig. 9 Observed power law rate expression and the order of reaction at different temperatures.

dione is higher second order in the lactic acid concentration, whereas the formation of acetic acid, propanoic acid and acetaldehyde is first order in the LA concentration.[51,56]

Consider the reaction as simply as possible, *i.e.*

$$2\mathrm{LA} \rightarrow 2,3\text{-pentanedione} + 2\mathrm{H_2O} + \mathrm{CO_2}$$

The rate of the reaction was calculated (Tables S2–S5, Fig. S8 and S9†) using the three equations shown below. Eqn (1)–(3) illustrate the rate, which is governed by the power law, absorption, and surface reactions. Each of these steps was considered as a rate-limiting step to the analysis of the actual RDS. The supplementary data also include additional rate expressions and a thorough derivation including a set of assumptions for the kinetic equations.

$$R_{(pC_3H_6O_3)} = K \cdot (p_{(C_8H_{10}O_3)})^m \quad (1)$$

$$R_A = K \cdot p_{(C_3H_{16}O_3)} \quad (2)$$

$$R_S = K(p2_{C_3H_{16}O_3} \cdot K_A)/[1 + p_{C_3H_{16}O_3} \cdot K_A]2 \quad (3)$$

Fig. S8† shows the observed ($R_{observed}$) and calculated ($R_{calculated}$) rate for all elementary steps. Based on the regression value, the graph provides evidence that the adsorption rate reaction offers the best fit for the dehydration of phenyl ethanol. However, since the reaction is catalysed by a heterogeneous catalyst, the surface reaction step is also regarded as the rate-determining phase. Thus, the Arrhenius equation for eqn (1)–(3) was derived, and the associated activation energy and pre-exponential factor were calculated for the actual rate-determining step.

The activation energy (E_a) of the process. Given the considerable variation in activation energies, it was likely that the adsorption step (Table 3) was the one that determined the rate.

Table 3 Observed activation energies and Arrhenius constant of the reactions

Rate expression	E_a (kJ mol^{-1})	Arrhenius constant
$R_{(pC_3H_6O_3)} = K{\cdot}(p_{C_8H_{10}O_3})^m$	94.2	5.2×10^{12}
$R_A = K{\cdot}p_{C_3H_{16}O_3}$	81.6	3.4×10^{11}
$R_S = K(p2_{C_3H_{16}O_3}{\cdot}K_A)/[1 + p_{C_3H_{16}O_3}{\cdot}K_A]2$	106.3	2.3×10^{13}

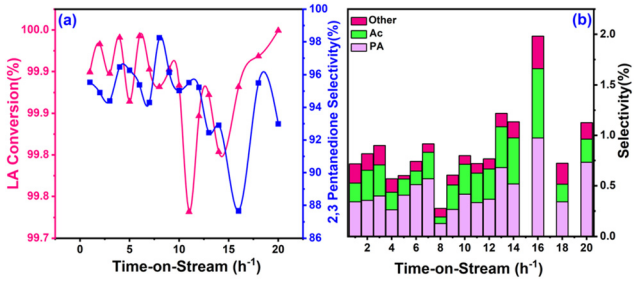

Fig. 10 (a) TOS on LA conversion and selectivity/rate of the formation of PON, (b) rate of formation of propanoic acid (PA), acetic acid (Ac), and others (acrylic acid, acetaldehyde, and so on.). Reaction conditions: catalyst, 1 g, 4.4% ZrO_2; feedstock, 40% (w); feed flow rate, 4.0 h^{-1}; carrier gas, 16 mL min^{-1}; and reaction temperature, 325 °C.

The slope and intercept of the relationship between $1/T$ and ln (k) were used to compute the E_a and pre-exponential factor. According to RDS, the adsorption of lactic acid on the catalyst surface controls the course of the entire reaction.

Evaluation of the stability and durability of the catalyst

The time-on-steam data showed no major deviation (Fig. 10a) in LA conversion until 20 h. At the same time, the selectivity toward 2,3-pentanedione was a bit shaky but grew progressively and steadily. For instance, the LA conversion and 2,3-pentanedione selectivity were 99.8% and 95.5%, respectively, at the beginning (1st hour) and reached 99.9% and 90.0%, respectively, by the end of 20th hour of operation. Fig. 10b displays a trace amount of propanoic acid, acetic acid, and other products detected during the reaction. These findings suggested that an increase in reaction time was accompanied by stability of the working catalytic. In general, the catalytic activity decreased considerably over time, which may be due to carbon deposits covering the active sites during the condensation of LA.[57] While ZrO_2 is known for its oxygen mobility through its lattice, the sufficient oxygen transfer to coke during the condensation of LA on the zirconia surface was indicated by a lower rate of carbon deposition.[58,59] The rate of coke deposition was calculated from TGA and found to be 4.5×10^{-3} g h^{-1}.

Discussion

According to kinetic studies, a higher LA concentration favoured 2,3-pentanedione selectivity, as the condensation

reaction is second order in LA concentration, where the dehydration toward acrylic acid follows a reverse trend.[7] Notably, under the current reaction conditions with the ZrO_2 catalyst, a 2,3-pentanedione selectivity of up to 74.1% was achieved compared to 1.1% (Table 2) for acrylic acid. The heat of reaction for those two reactions was determined (in Table S6†) by Gunter *et al.*[51] and served as evidence to validate our results. According to the chemical thermodynamics, increasing the process temperature is more favourable for endothermic reactions than for exothermic ones. Likewise, an increase in the process temperature favours processes with a high activation energy.[17] Since the activation energy of the primary reaction is lower than that of the side reactions, this can only be satisfied with the observed E_a for catalytic conversion of LA (81.6 kJ mol^{-1}).[17,54] Based on these two considerations, increasing reaction temperature should favour the dehydration step to acrylic acid but is unfavourable to the condensation to 2,3-pentanedione. This fact is also confirmed by the trend of the selectivity of 2,3-pentanedione, which decreased after 325 °C (Fig. 7a). In contrast, in our previous study, we found that the selectivity of acrylic acid depends on the reaction temperature.[7] Inline, the best yield of 2,3-pentanedione (95.3%) was found at 325 °C over the ZrO_2 catalyst.

A possible reaction mechanism for the formation of 2,3-pentanedione over ZrO_2 was proposed and is shown in Scheme 1. The postulated mechanism supports the earlier reported work[15,49,50] and is based on the experimental evidence, DFT calculations, and kinetic studies presented in the current work. It has been observed that there are primarily three steps involved in the synthesis of 2,3-pentanedione: dehydration, decarboxylation, and then again dehydration. The basic sites of ZrO_2 first attack the H atom of the –COOH group of lactic acid to generate an enolate ***E-1*** (intermediate **3**, as shown in Scheme 1) through proton transfer. Subsequently, the enolate (***E-1***) attacks another lactic acid molecule to produce intermediate **5** and rearranges it, noting the first dehydration step to form intermediate **7**. The process then proceeds *via* ketonic decarboxylation (the elimination of CO_2 from carboxylic acid)[60,61] and produces enolate (E-2). We measured the gaseous product directly after the reaction *via* an online GC-RGA and found a significant presence of CO_2 with a trace of CO and H_2 (Table S5†). This provides direct confirmation of the decarboxylation process that has taken place. Enolate (***E-2***) was then rearranged to intermediate **11** *via* ketonic decarboxylation of carboxylic acids using the beta-keto acid acidic sites, thereby eliminating molecular water (dehydration) and forming another enolate (***E-3***).[62] Successively, the enolate (***E-3***) (I3) isomerises into 2,3-pentanedione and desorbs from the ZrO_2 surface.

To further substantiate our experimental results, density functional theory (DFT) simulations were performed to calculate the change in the electronic structure of molecules during the condensation of LA over the ZrO_2 nanocluster. As shown in Fig. 11, lactic acid has three potential adsorption sites on the ZrO_2 surface, namely, the oxygen atom in the alcohol functional group and the two oxygen atoms in the carboxyl group.

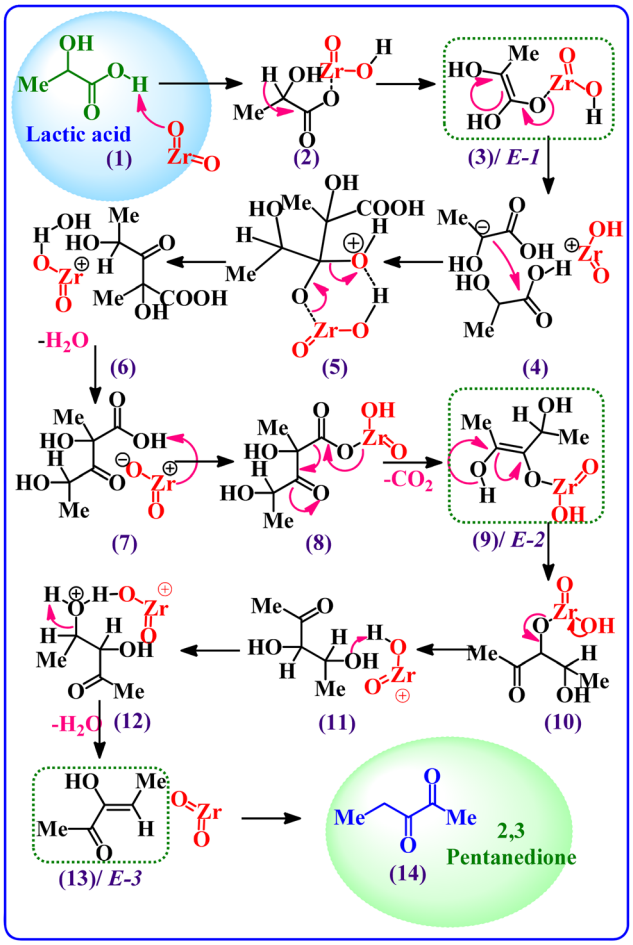

Scheme 1 Possible mechanism of 2,3-pentanedione formation from lactic acid over polymorphic ZrO_2.

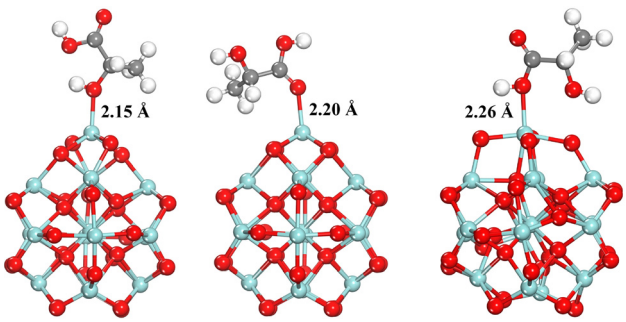

Fig. 11 Optimised structures of lactic acid adsorbed on the ZrO_2 nanocluster *via* (a) the oxygen atom of the alcohol functional group and (b and c) the carboxyl group. Here, white, red, grey, and cyan colour balls represent hydrogen, oxygen, carbon, and zirconium atoms, respectively.

Adsorption involving a double-bonded oxygen atom and a single-bonded hydroxyl group shows binding energies of −1.48 and −1.23 eV, respectively, with Zr–O bond lengths of about 2.21 and 2.26 Å. On the other hand, the adsorption energy of LA over the ZrO_2 nanocluster, involving the oxygen atom of the

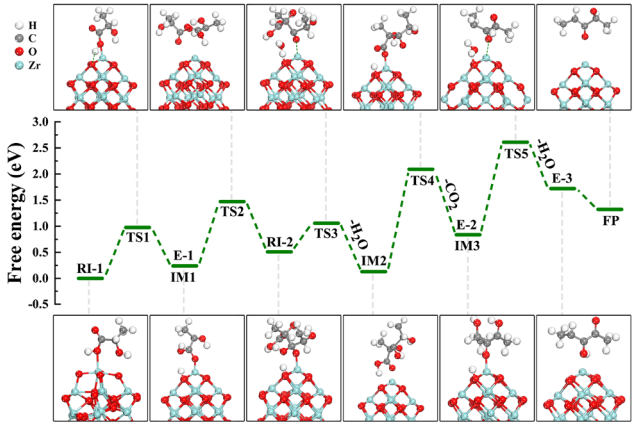

Fig. 12 Computed free energy profile and the corresponding optimised structures for LA to 2,3-PD conversion on the ZrO_2 nanocluster. Here, white, grey, red, and cyan balls indicate hydrogen, carbon, oxygen, and zirconium atoms, respectively.

alcohol functional group, is −1.61 eV with a Zr–O bond length of 2.15 Å.

The observed chemisorption had an impact on the nearest C–O bond in LA, leading to an expansion in the bond length to 1.39 Å from its pristine 1.35 Å.

The reaction pathway initiates with the adsorption of LA *via* the oxygen atom of the carboxylic functional group on the ZrO_2 nanocluster. Fig. 12 shows the optimised configurations of reactive sites for condensation of LA to 2,3-pentanedione on the ZrO_2 nanocluster, as well as the corresponding free energy profile. Here, the adsorption of LA (the reaction intermediate (**RI-1**)) occurs *via* the oxygen atom of the carboxylic functional group on the ZrO_2 nanocluster to form IM1 (formation of first enolate ***E-1***) by proton transfer through transition state TS1 with a relative energy barrier of 0.98 eV. Another LA molecule attacks the IM1 to produce **RI-2** *via* transition state TS2 with a relative energy barrier of 1.23 eV. Subsequently, the first H_2O molecule is eliminated through TS3, leading to the formation of IM2. The process then proceeds to form IM3 (formation of the second enolate (***E-2***)) through TS4 with a relative energy of 1.96 eV *via* ketonic decarboxylation (the elimination of CO_2 from carboxylic acid). Second, the enolate (***E-2***) is rearranged to a new intermediate through TS5 with a reaction energy barrier of 1.77 eV. Following this, a water molecule is liberated and forms the third enolate (***E-3***). ***E-3*** isomerism leads to the formation of the final product (FP) 2,3-pentanedione and completes the catalytic cycle.

Conclusions

The results of this study indicate that the zirconium oxide catalyst has good activity and stability for the vapor-phase condensation of bio-derived lactic to 2,3-pentanedione with 99.7% conversion and 95.5% selectivity at 325 °C. Two key steps are involved in the synthesis of 2,3-pentanedione from LA: decarboxylation of LA and ketonisation with water loss. The catalysed decarboxylation process requires basic sites, whereas the catalysed ketonisation with water loss reaction requires acidic sites. In other words, a bifunctional ZrO_2 catalyst with both acidic and basic sites on its surface has a high potential for catalysing the condensation of LA to 2,3-pentanedione. Furthermore, the kinetic study indicated that the entire reaction is dominated by LA adsorption on the catalyst surface, with LA adsorption being the rate-limiting step and second-order reaction in lactic acid concentration. The activation energy was found to be 81.6 kJ mol^{-1} using the Arrhenius equation. The influence of acid–base chemistry on the condensation of LA to 2,3-pentanedione should be investigated for bio-based fine chemicals for future research on bio-refinery and process.

Conflicts of interest

There are no conflicts to declare.

Acknowledgements

This work was supported by the Council of Scientific & Industrial Research (CSIR) New Delhi through Focused Based Research (CLP-FBR) (project no. MLP-1169). N. D. is thankful to the Council of Scientific & Industrial Research (CSIR), New Delhi, for the financial support in the form of an SRF. The authors are grateful to the Analytical Science Division, Nano Catalysis Area, and Biochemistry & Biotechnology Area for providing analytical and physicochemical characterisation services.

References

1 G. W. Huber, S. Iborra and A. Corma, *Chem. Rev.*, 2006, **106**, 4044–4098.
2 H. Bai, W. Yi, J. Li, G. Xi, Y. Li, H. Yang and J. Liu, *J. Mater. Chem. A*, 2016, **4**, 1566–1571.
3 C. M. Tang, J. S. Peng, X. L. Li, Z. J. Zhai, W. Bai, N. Jiang, H. J. Gao and Y. W. Liao, *Green Chem.*, 2015, **17**, 1159–1166.
4 L. Li, G. Liu, Y. Li, Z. Zhu, H. Xu, J. Chen and X. Ren, *ACS Omega*, 2020, **5**, 30001–30010.
5 H. Zhang, H. Li and S. Yang, in *Biomass, Biofuels, Biochemicals*, ed. S. Saravanamurugan, A. Pandey, H. Li and A. Riisager, Elsevier, 2020, pp. 227–257, DOI: **10.1016/b978-0-444-64307-0.00008-1**.
6 R. Goyal, O. Singh, A. Agrawal, C. Samanta and B. Sarkar, *Catal. Rev.*, 2020, **64**, 229–285.
7 N. Dhiman, S. R. Yenumala, D. Agrawal, A. Pandey, J. Porwal and B. Sarkar, *Chem. Eng. J.*, 2023, **466**, 143240.
8 O. Singh, T. Sharma, I. Ghosh, D. Dasgupta, B. P. Vempatapu, S. Hazra, A. L. Kustov, B. Sarkar and D. Ghosh, *ACS Sustainable Chem. Eng.*, 2019, **7**, 13437–13445.
9 P. Baral, A. Pundir, V. Kumar, A. K. Kurmi and D. Agrawal, *Food Bioprod. Process.*, 2020, **124**, 72–81.

10 K. M. Nampoothiri, N. R. Nair and R. P. John, *Bioresour. Technol.*, 2010, **101**(22), 8493–8501.
11 H. J. Cho, C. C. Chang and W. Fan, *Green Chem.*, 2014, **16**, 3428–3433.
12 Z. Jia, C. Tang, K. Ma and X. Li, *Chem. Commun.*, 2023, **59**, 9235–9238.
13 Y. Wang, C. Tang, K. Ma and X. Li, *Surf. Interfaces*, 2023, **42**, 103524.
14 Z. Jia, R. Liu, X. Li, Z. Chen, Y. Wang, K. Ma and C. Tang, *Surf. Interfaces*, 2023, **39**, 102888.
15 X. L. Li, L. W. Sun, W. X. Zou, P. Cao, Z. Chen, C. M. Tang and L. Dong, *ChemCatChem*, 2017, **9**, 4621–4627.
16 *The chemistry and technology of furfural and its many by-products*, ed. K. J. Zeitsch, Elsevier, 2000, vol. 13, pp. 120–149.
17 L. W. Sun, X. L. Li and C. M. Tang, *Acta Phys.-Chim. Sin.*, 2016, **32**, 2327–2336.
18 X. L. Li, Y. Zhang, Z. Chen, P. Can, W. X. Zou, C. M. Tang, L. Dong and Y. Wang, *Ind. Eng. Chem. Res.*, 2017, **56**, 14437–14446.
19 V. C. Ghantani, S. T. Lomate, M. K. Dongare and S. B. Umbarkar, *Green Chem.*, 2013, **15**, 1211–1217.
20 J. F. Zhang, X. Z. Feng, Y. L. Zhao, W. J. Ji and C. T. Au, *J. Ind. Eng. Chem.*, 2014, **20**, 1353–1358.
21 G. C. Gunter, R. Craciun, M. S. Tam, J. E. Jackson and D. J. Miller, *J. Catal.*, 1996, **164**, 207–219.
22 L. Huang, M. H. Wai and S. Kawi, *React. Chem. Eng.*, 2023, **8**, 502–537.
23 S. S. Barton, M. J. B. Evans, E. Halliop and J. A. F. MacDonald, *Carbon*, 1997, **35**, 1361–1366.
24 P. Baral, M. Munagala, Y. Shastri, V. Kumar and D. Agrawal, *Cellulose*, 2021, **28**, 6305–6322.
25 G. Kresse and J. Furthmuller, *Phys. Rev. B: Condens. Matter Mater. Phys.*, 1996, **54**, 11169–11186.
26 J. P. Perdew, K. Burke and M. Ernzerhof, *Phys. Rev. Lett.*, 1996, **77**, 3865–3868.
27 P. E. Blochl, *Phys. Rev. B: Condens. Matter Mater. Phys.*, 1994, **50**, 17953–17979.
28 S. Grimme, J. Antony, S. Ehrlich and H. Krieg, *J. Chem. Phys.*, 2010, **132**, 154104.
29 R. Goyal, B. M. Abraham, O. Singh, S. Sameer, R. Bal and P. Mondal, *Renewable Energy*, 2022, **183**, 791–801.
30 R. A. L. Baylon, J. M. Sun, L. Kovarik, M. Engelhard, H. Q. Li, A. D. Winkelman and Y. Wang, *Appl. Catal., B*, 2018, **234**, 337–346.
31 C. Temple Jr and J. A. Montgomery, *J. Org. Chem.*, 1963, **28**, 3038–3041.
32 A. E. Nelson and K. H. Schulz, *Appl. Surf. Sci.*, 2003, **210**, 206–221.
33 S. Kumar, M. M. Devi, S. K. Kansal and S. Saravanamurugan, *Catal. Sci. Technol.*, 2020, **10**, 7016–7026.
34 A. Agrawal, O. Singh, B. M. Abraham, S. R. Yenumala, A. Ray and B. Sarkar, *Fuel Process. Technol.*, 2022, **235**, 107362.
35 C. Wagner, A. Naumkin, A. Kraut-Vass, J. Allison, C. Powell and J. J. Rumble, *Available online*: **http://srdata.nist.gov/xps/** *(accessed on 12 May 2022)*, 2003.
36 L. P. C. Silva, L. E. Terra, A. C. S. L. S. Coutinho and F. B. Passos, *J. Catal.*, 2016, **341**, 1–12.
37 I. Prymak, V. N. Kalevaru, S. Wohlrab and A. Martin, *Catal. Sci. Technol.*, 2015, **5**, 2322–2331.
38 E. M. Albuquerque, L. E. P. Borges, M. A. Fraga and C. Sievers, *ChemCatChem*, 2017, **9**, 2675–2683.
39 S. Wang and E. Iglesia, *J. Phys. Chem. C*, 2017, **121**, 18030–18046.
40 B.-Q. Xu, T. Yamaguchi and K. Tanabe, *Chem. Lett.*, 1988, **17**, 1663–1666.
41 C. O. Chikere, N. H. Faisal, P. Kong-Thoo-Lin and C. Fernandez, *Nanomaterials*, 2020, **10**, 537.
42 D. Prakashbabu, R. Hari Krishna, B. M. Nagabhushana, H. Nagabhushana, C. Shivakumara, R. P. Chakradar, H. B. Ramalingam, S. C. Sharma and R. Chandramohan, *Spectrochim. Acta, Part A*, 2014, **122**, 216–222.
43 N. A. S. Din, S. J. Lim, M. Y. Maskat, S. A. Mutalib and N. A. M. Zaini, *Bioresour. Bioprocess.*, 2021, **8**, 31.
44 L. Zhang, D. S. Theng, Y. Du, S. Xi, L. Huang, F. Gao, C. Wang, L. Chen and A. Borgna, *Catal. Sci. Technol.*, 2017, **7**, 6101–6111.
45 N. Sobuś and I. Czekaj, *Catal. Today*, 2022, **387**, 172–185.
46 S. Ding, J. Zhao and Q. Yu, *Catalysts*, 2019, **9**, 768.
47 X. Yang, X. Yu, M. Lin, M. Ge, Y. Zhao and F. Wang, *J. Mater. Chem. A*, 2017, **5**, 13799–13806.
48 D. C. Hurum, A. G. Agrios, K. A. Gray, T. Rajh and M. C. Thurnauer, *J. Phys. Chem. B*, 2003, **107**, 4545–4549.
49 X. Li, Y. Zhang, Z. Chen, P. Cao, W. Zou, C. Tang, L. Dong and Y. Wang, *Ind. Eng. Chem. Res.*, 2017, **56**, 14437–14446.
50 G. C. Gunter, D. J. Miller and J. E. Jackson, *J. Catal.*, 1994, **148**, 252–260.
51 G. C. Gunter, D. J. Miller and J. E. Jackson, *J. Catal.*, 1994, **148**, 252–260.
52 J. Liu, P. Xu, P. Wang, Z. Xu, X. Feng, W. Ji and C.-T. Au, *Sci. Rep.*, 2019, **9**, 16988.
53 Q. Gao, K. Zheng, C. Li, J. Wang, G. Zhang, Q. Zhang, F. Song, T. Zhang, J. Zhang and Y. Han, *Chem. Commun.*, 2023, **59**, 1489–1492.
54 D. C. Wadley, M. S. Tam, P. B. Kokitkar, J. E. Jackson and D. J. Miller, *J. Catal.*, 1997, **165**, 162–171.
55 X. Li, L. Sun, W. Zou, P. Cao, Z. Chen, C. Tang and L. Dong, *ChemCatChem*, 2017, **9**, 4621–4627.
56 G. C. Gunter, R. H. Langford, J. E. Jackson and D. J. Miller, *Ind. Eng. Chem. Res.*, 1995, **34**, 974–980.
57 J. Zhang, J. Lin and P. Cen, *Can. J. Chem. Eng.*, 2008, **86**, 1047–1053.
58 L. Yang, X. Gu, L. Tan, L. Zhang, C. Wang and N. Xu, *Sep. Purif. Technol.*, 2003, **32**, 301–306.
59 Z. Si, D. Weng, X. Wu, Z. Ma, J. Ma and R. Ran, *Catal. Today*, 2013, **201**, 122–130.
60 I. L. Simakova and D. Y. Murzin, *J. Energy Chem.*, 2016, **25**, 208–224.
61 A. Pulido, B. Oliver-Tomas, M. Renz, M. Boronat and A. Corma, *ChemSusChem*, 2013, **6**, 141–151.
62 J. ten Dam, K. Djanashvili, F. Kapteijn and U. Hanefeld, *ChemCatChem*, 2013, **5**, 497–505.

